

Supplementary Material

Keke Ying

Abstract

This document is the supplementary material for the article “Reconfigurable Massive MIMO: Precoding Design and Channel Estimation in the Electromagnetic Domain”.

I. COMPARISON BETWEEN RMMIMO AND TMMIMO ARCHITECTURES

Fig. 1 presents a comparison of four different structures: (a) Traditional fully-digital array (referred to as TmMIMO in this paper); (b) Reconfigurable fully-digital array (referred to as RmMIMO in this paper); (c) Traditional hybrid array [R1]; and (d) Reconfigurable hybrid array.

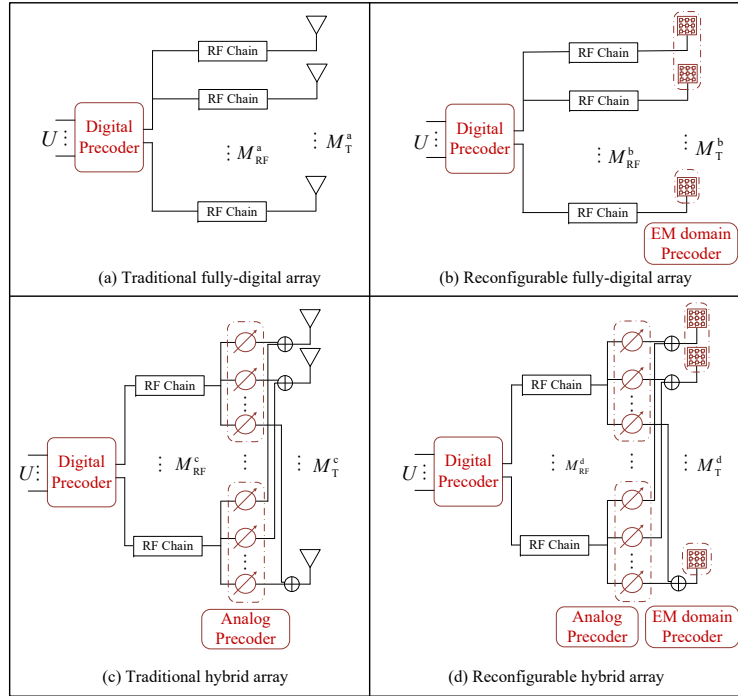


Fig. 1. A comparison of traditional fully-digital/hybrid arrays and their reconfigurable counterparts in this paper.

Fig. 1 demonstrates that the primary difference between the reconfigurable and traditional arrays lies in the antenna configuration. This paper compares configurations (a) and (b) to assess

the additional benefits provided by reconfigurable antenna radiation patterns. We define the ability to customize radiation patterns as EM domain precoding, distinguishing it from traditional digital and analog precoding. Furthermore, our architecture, although distinct from the traditional hybrid array (c), remains compatible with it. Specifically, by replacing the antennas in the traditional hybrid array with reconfigurable antennas, we derive structure (d).

To ensure a fair comparison between the performance of the proposed framework and existing architectures, it is crucial to maintain consistency in certain dimensions. We consider the following two cases:

(1) All architectures have the same number of antennas ($M_T^a = M_T^b = M_T^c = M_T^d$):

- Based on our simulation results in the manuscript, structure (b) outperforms structure (a) in terms of SE. Additionally, existing research has confirmed that structure (a) outperforms structure (c) in SE when the number of antennas is the same [R1], as hybrid arrays typically employ fewer RF chains than antennas. Therefore, the relative SE performance is $b > a > c$.
- Similarly, with the same number of antennas, and due to the higher degrees of freedom (DoF) in a fully digital array compared to hybrid beamforming, we have $b > d$. Furthermore, the introduction of additional EM domain DoFs by RmMIMO naturally results in $d > c$, leading to an overall relationship of $b > d > c$.
- The relative performance between (a) and (d) depends on various factors, such as the number of user equipment (UEs), the design DoF of the antenna radiation pattern, and the adopted precoding algorithm. This issue requires further research and is beyond the scope of this paper.

(2) All architectures have the same number of RF chains ($M_{\text{RF}}^a = M_{\text{RF}}^b = M_{\text{RF}}^c = M_{\text{RF}}^d$):

- Similar to the previous analysis, the potential SE performance bound is determined by the design DoF. Thus, we have $d > b > a$ and $d > c > a$.
- Next, we compare the performance of structures (b) and (c). In this case, the number of antennas in the proposed structure (b) equals the number of RF chains (i.e., $M_T^b = M_{\text{RF}}^b$), while the number of antennas in the traditional structure (c) exceeds the number of RF chains (i.e., $M_T^c \geq M_{\text{RF}}^c$). From an SE perspective, directly comparing architectures (b) and (c) would be influenced by the adopted hybrid precoding algorithms. Therefore, we compare their performance indirectly.

Figure 2 compares architectures (a) and (b) with the same number of RF chains (and

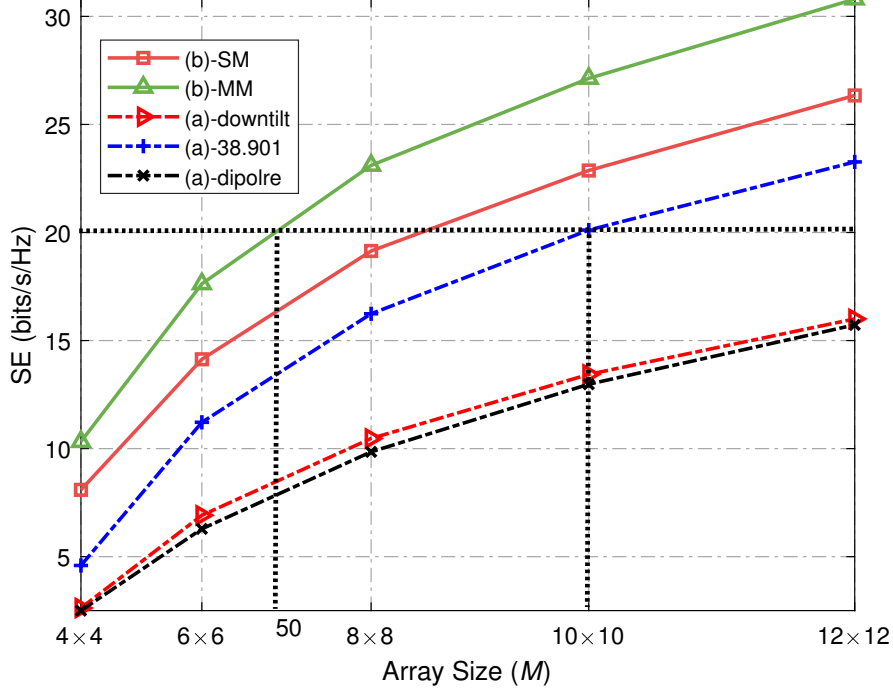


Fig. 2. SE versus array size M for architecture (a) and (b) when $U = 6$, $K = 100$, $\text{SNR}_u = 10\text{dB}$, $\text{SNR}_d = 15\text{dB}$.

the same number of antennas). The simulation results indicate that, to achieve the same SE, architecture (b) requires fewer antennas than architecture (a). For instance, at an SE of 20 bits/s/Hz, architecture (b)-MM with approximately 50 antennas achieves equivalent performance to architecture (a)-38.901 with a 10×10 antenna configuration. On the other hand, for architecture (c)-38.901 with 50 RF chains and a 10×10 antenna configuration, its performance is evidently inferior to that of architecture (a)-38.901 with the same number of antennas. Thus, it can be inferred that if we were to plot the performance curves of architecture (c)-38.901 with different numbers of antennas (but a fixed number of RF chains at 50), when the number of antennas M_T^c exceeds 50, the SE performance curve should be no higher than that of architecture (a)-38.901. **This also confirms that, with the same number of RF chains, architecture (b) can at least match the performance of architecture (c) with more antennas. The relative SE performance relationship can be inferred from Fig. 2.**

II. VISUALIZATION OF OPTIMIZED RADIATION PATTERNS

Following a progressive process from simple to complex channel scenarios, we compared the visual results of the optimized radiation patterns for multiple-user transmissions.

- In Fig. 3, we consider a single-mode (SM), line-of-sight (LoS)-dominant (the Rice factor is set to 15 dB) scenario for 3-UE transmission, examining differences in radiation patterns for various values of K . The optimized radiation pattern is shown in Fig. 14. The colored arrows denote the angle of departure at the BS for different UEs. In this case, it is evident that the pattern optimization strategy primarily focuses on energy harvesting, aiming to gather as much channel energy as possible from the UEs' main multipath directions. As K increases, the radiation pattern exhibits greater directivity, enabling finer beam steering towards corresponding users and enhancing the received energy for each path.

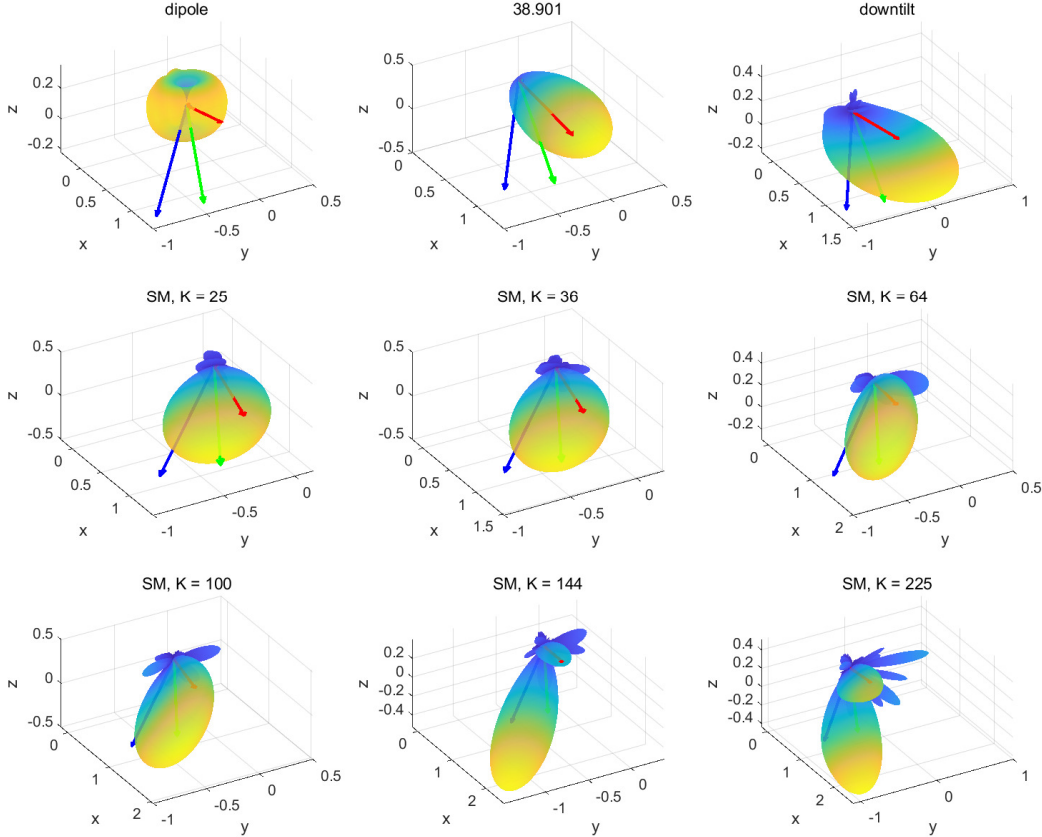


Fig. 3. Optimized patterns for a 3 UE, SM, LoS-dominated transmission scenario.

- In Fig. 4, we investigate the multi-mode(MM), LoS-dominated scenario, comparing radiation pattern differences across various antennas. It is observed that the radiation patterns on

different antennas focus on different paths, thereby achieving better overall receiving energy across all directions.

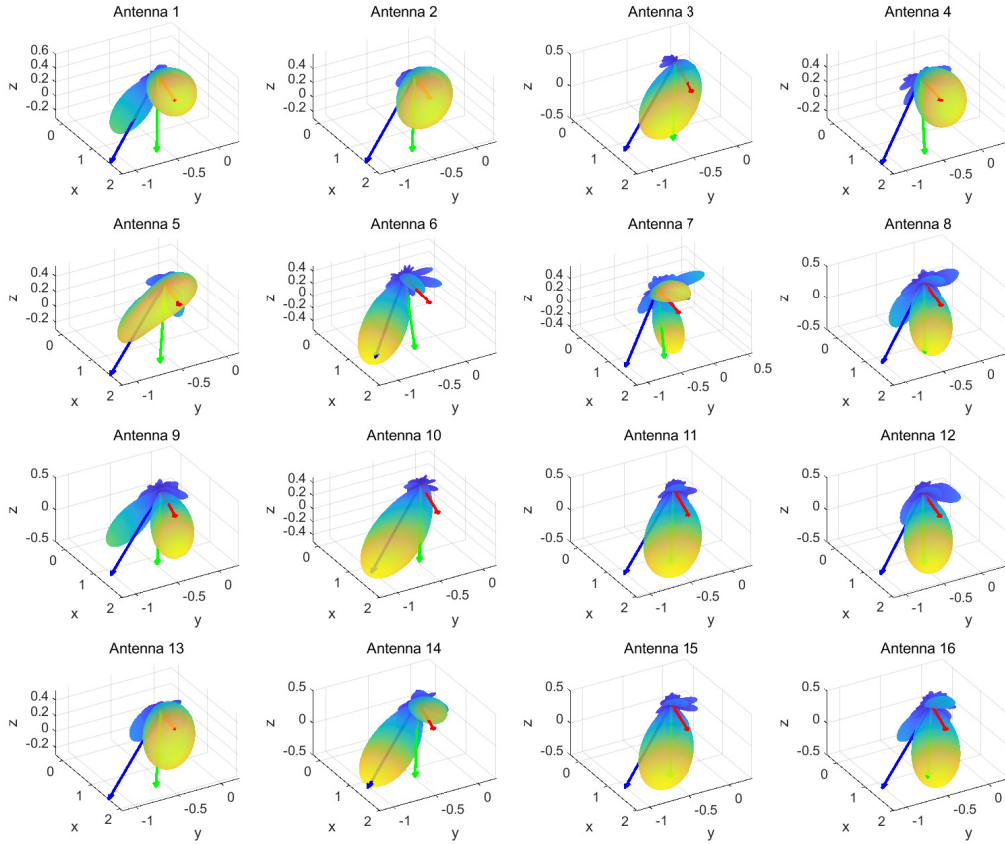


Fig. 4. Optimized pattern for a 3 UE, MM, LoS-dominated transmission scenario, where the BS is equipped with a 4×4 RmMIMO.

- In Fig.5, we analyze the SM, non-line-of-sight (NLoS) transmission, assuming each UE has 8 paths, for 2-UE transmission. In this context, the design of the radiation pattern does not consider all paths for each UE but selectively focuses on certain paths. Additionally, as K increases, the beam's directivity progressively strengthens.

Overall, the proposed scheme for optimizing radiation patterns is an energy harvesting strategy. For LoS-dominated propagation scenarios, whether in SM or MM cases, the radiation pattern is optimized to capture as much energy as possible from all user main paths. The higher the order of spherical harmonics, the stronger the directivity of the designed beam. For MM scenarios, different antennas' radiation patterns focus on different receiving path angles. For NLoS scenarios, since there is no obvious main path, the optimized radiation pattern selectively

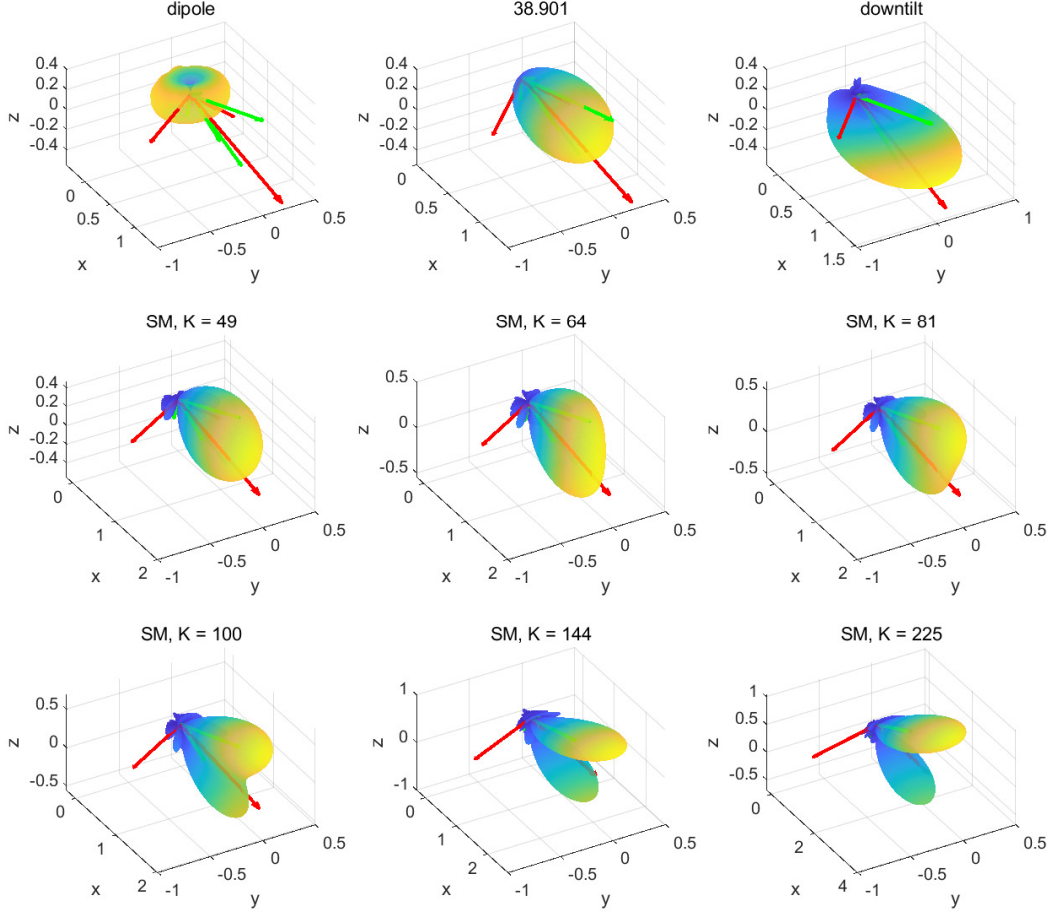


Fig. 5. Optimized patterns for a 2 UE, SM, NLoS transmission scenario.

receives part of the paths rather than considering all of them. Similarly, as the order of spherical harmonics increases, the directivity of the designed beam also strengthens.

III. COMPARISON BETWEEN REAL PATTERN AND COMPLEX PATTERN

This paper considers antenna radiation pattern functions that are real-valued due to the emphasis on amplitude information in existing literature. For instance, the radiation patterns outlined in 3GPP 38.901 [R3] and Hertz dipole radiation patterns are real-valued. To ensure a fair comparison, our study also focuses solely on the optimization of real-valued radiation pattern functions.

The study referenced in [R2] incorporates phase information in the radiation pattern because the parasitic array structure introduces an additional array factor to the initial patch antenna radiation pattern. The amplitude and phase characteristics of this array factor arise from the

parasitic array structure's design. In our paper, we aim to directly design the required radiation pattern amplitude (and phase) characteristics to match the channel environment. Deriving the corresponding array structure design from our optimized radiation pattern function is beyond this study's scope.

Given the above explanation, we will now discuss how to extend our proposed solution to the scenario of complex radiation pattern optimization. The approach is straightforward. In the original paper, we utilized real-form spherical harmonic functions to orthogonally decompose the radiation pattern function, i.e.,

$$f(\theta, \phi) = \sum_{k=1}^K \alpha_k \omega_k(\theta, \phi), \quad (4)$$

where $\omega_k(\theta, \phi) = Y_c^r(\theta, \phi)$, $k = c^2 + c + r + 1$, $c \in [0, +\infty]$, $r \in [-c, c]$, with the real spherical harmonic function $Y_c^r(\theta, \phi)$ given by

$$Y_c^r(\theta, \phi) = \begin{cases} (-1)^r \sqrt{2} K_c^r \cos(r\varphi) P_c^r(\cos \theta) & 0 < r \leq c, \\ (-1)^r \sqrt{2} K_c^r \sin(-r\varphi) P_c^{-r}(\cos \theta) & -c \leq r < 0, \\ K_c^0 P_c^0(\cos \theta) & r = 0. \end{cases} \quad (5)$$

where $K_c^r = \sqrt{\frac{2c+1}{4\pi} \frac{(c-|r|)!}{(c+|r|)!}}$. Similar to the discrete cosine transform (DCT) and discrete Fourier transform (DFT) used in one-dimensional signals, we can also apply the complex form of spherical harmonic functions for the decomposition of complex radiation patterns, i.e.,

$$Y_c^r(\theta, \varphi) = (-1)^r \sqrt{\frac{(2c+1)(c-r)!}{4\pi(c+r)!}} P_c^r(\cos \theta) e^{ir\varphi}, c \in [0, +\infty], r \in [-c, c]. \quad (E2)$$

Then, our precoding problem can still be expressed as shown in Equation (10) of the manuscript. However, for the single-mode (SM) case, the manifold constraint on the radiation pattern expansion coefficient α_m shifts from the real sphere manifold $\mathcal{S} = \{\alpha \in \mathbb{R}^K : \|\alpha\|_2 = 1\}$ to the complex sphere manifold (E3). Similarly, for the multi-mode (MM) case, the original real oblique manifold $\mathcal{OB} = \{\mathbf{A} \in \mathbb{R}^{\tilde{K} \times M} : [\mathbf{A}^T \mathbf{A}]_{m,m} = 1, \forall m\}$ becomes a complex oblique manifold (E4).

$$\begin{aligned} & \max_{\{\alpha_m\}_{m=1}^M, \{\mathbf{w}_g\}_{g=1}^G} R \\ & \text{s.t.} \quad \|\alpha_m\|^2 = 1, \forall m, \\ & \quad \sum_{g=1}^G \|\mathbf{w}_g\|_{\text{F}}^2 \leq P_T. \end{aligned} \quad (10)$$

$$\mathcal{S} = \{\boldsymbol{\alpha} \in \mathbb{C}^K : \|\boldsymbol{\alpha}\|_2 = 1\}. \quad (\text{E3})$$

$$\mathcal{OB} = \{\boldsymbol{\Lambda} \in \mathbb{C}^{\tilde{K} \times M} : [\boldsymbol{\Lambda}^H \boldsymbol{\Lambda}]_{m,m} = 1, \forall m\}. \quad (\text{E4})$$

After defining the complex manifold, we can still apply the method described in this paper to compute the Riemannian gradient and utilize the alternating optimization approach to calculate the EM domain precoder and digital domain precoder. Specifically, the required Euclidean gradient for complex radiation pattern optimization in the SM case is given by (E5).

$$\nabla f(\boldsymbol{\alpha}_l) = - \sum_{g=1}^G \sum_{u=1}^U \frac{\boldsymbol{\chi}_{u,g}^{\iota,(1)} - \boldsymbol{\chi}_{u,g}^{\iota,(2)}}{\ln 2}, \quad (\text{E5})$$

where $\boldsymbol{\chi}_{u,g}^{\iota,(1)} \triangleq \frac{\xi \boldsymbol{\alpha}_l^T (\mathbf{Q}_{u,g} \mathbf{W}_g^\iota (\mathbf{W}_g^\iota)^H \mathbf{Q}_{u,g}^H)^T}{1 + \xi \|\boldsymbol{\alpha}_l^H \mathbf{Q}_{u,g} \mathbf{W}_g^\iota\|_2^2}$ and $\boldsymbol{\chi}_{u,g}^{\iota,(2)} \triangleq \frac{\xi \boldsymbol{\alpha}_l^T (\mathbf{Q}_{u,g} \mathbf{W}_{u,g}^\iota (\mathbf{W}_{u,g}^\iota)^H \mathbf{Q}_{u,g}^H)^T}{1 + \xi \|\boldsymbol{\alpha}_l^H \mathbf{Q}_{u,g} \mathbf{W}_{u,g}^\iota\|_2^2}$. Specifically, $\mathbf{W}_{u,g}^\iota = [\mathbf{w}_{1,g}^\iota, \dots, \mathbf{w}_{u-1,g}^\iota, \mathbf{w}_{u+1,g}^\iota, \mathbf{w}_{U,g}^\iota] \in \mathbb{C}^{M \times (U-1)}$ is composed of the precoding vectors for all U UEs except for $\mathbf{w}_{u,g}^\iota$. Meanwhile, the the Euclidean gradient for complex radiation pattern optimization in MM case is given by (E6).

$$\nabla f(\boldsymbol{\Lambda}_l) = \left(- \sum_{g=1}^G \sum_{u=1}^U \frac{\boldsymbol{\Gamma}_{u,g}^{\iota,(1)} - \boldsymbol{\Gamma}_{u,g}^{\iota,(2)}}{\ln 2} \right) \odot \mathbf{M}_0, \quad (\text{E6})$$

where $\boldsymbol{\Gamma}_{u,g}^{\iota,(1)} \triangleq \frac{\xi (\mathbf{q}_{u,g} \mathbf{q}_{u,g}^H)^T \boldsymbol{\Lambda}_l^* (\mathbf{W}_g^\iota (\mathbf{W}_g^\iota)^H)^T}{1 + \xi \|\mathbf{q}_{u,g}^H \boldsymbol{\Lambda}_l \mathbf{W}_g^\iota\|_2^2}$, $\boldsymbol{\Gamma}_{u,g}^{\iota,(2)} \triangleq \frac{\xi (\mathbf{q}_{u,g} \mathbf{q}_{u,g}^H)^T \boldsymbol{\Lambda}_l^* (\mathbf{W}_{u,g}^\iota (\mathbf{W}_{u,g}^\iota)^H)^T}{1 + \xi \|\mathbf{q}_{u,g}^H \boldsymbol{\Lambda}_l \mathbf{W}_{u,g}^\iota\|_2^2}$, and \mathbf{M}_0 is a mask block diagonal matrix defined as $\mathbf{M}_0 = \text{Blkdiag}\{\mathbf{m}_1, \dots, \mathbf{m}_M\} \in \mathbb{R}^{\tilde{K} \times M}$, and $\mathbf{m}_1 = \mathbf{m}_2 = \dots = \mathbf{m}_M = \mathbf{1}_K$.

To evaluate the additional degrees of freedom (DoF) achieved through radiation phase design, we compared the performance of real pattern optimization and complex pattern optimization. Fig. 6 illustrates the SE performance of various precoding schemes as a function of downlink precoding signal-to-noise ratio (SNR_d). In this simulation, we assume $U = 6$, $M = 6 \times 6$, $K = 100$, and $J = 24$. We assume perfect eCSI and sCSI for RmMIMO and TmMIMO systems, respectively. **In the MM scenario, complex pattern optimization demonstrates additional performance gain over real pattern optimization. For the SM optimization, the extra phase DoF results in little SE gain.** This is likely due to the difficulty in identifying a common radiation pattern whose phase can adapt to various antennas in SM case. By contrast, MM optimization successfully addresses this issue by assigning antenna-specific complex patterns.

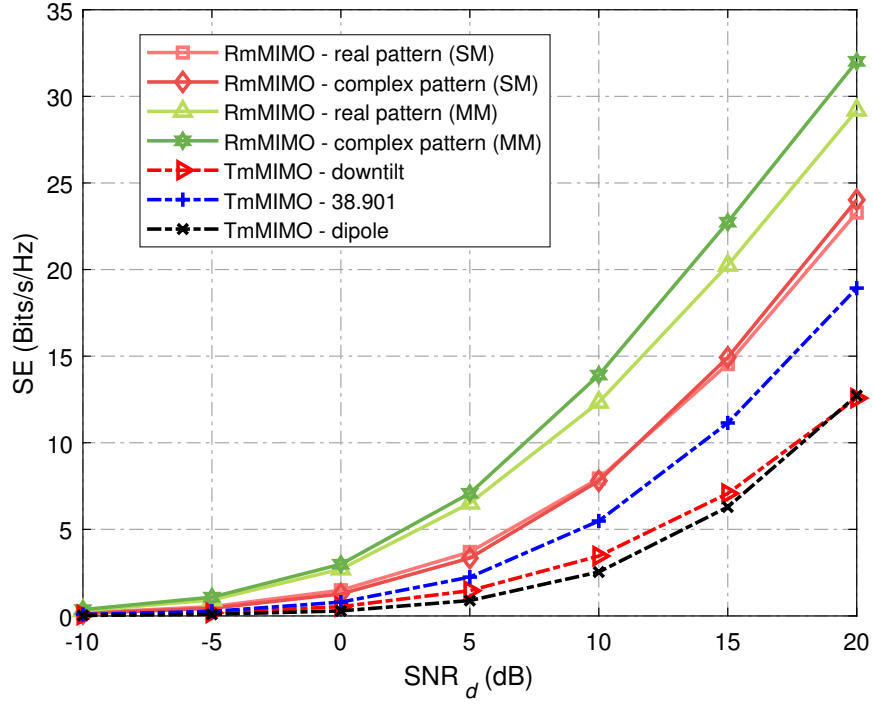


Fig. 6. SE versus SNR_d for RmMIMO and TmMIMO when $U = 6$, $M = 6 \times 6$, $K = 100$, and $J = 24$.

REFERENCES

- [R1] A. Alkhateeb and R. W. Heath, "Frequency selective hybrid precoding for limited feedback millimeter wave systems," *IEEE Trans. Commun.*, vol. 64, no. 5, pp. 1801-1818, May 2016.
- [R2] M. A. Towfiq, I. Bahceci, S. Blanch, J. Romeu, L. Jofre and B. A. Cetiner, "A reconfigurable antenna with beam steering and beamwidth variability for wireless communications," *IEEE Trans. Antennas Propag.*, vol. 66, no. 10, pp. 5052-5063, Oct. 2018.
- [R3] 3GPP, "Study on channel model for frequencies from 0.5 to 100 GHz," 3rd Generation Partnership Project (3GPP), Technical Report (TR) 38.901, 05 2017, version 14.0.0.